

Precision aerosol-jet micropatterning of liquid metal for high-performance flexible strain sensors

Received: 27 October 2024

Accepted: 1 August 2025

Published online: 25 August 2025

Benyan Xu¹, Mingyang Yang¹, Wenjun Cheng¹, Xuyin Li¹, Ximei Xu¹, Wenming Li¹, Hao Zhang¹ & Ming Zhou^{1,2} ✉

Flexible wearable strain sensors are rapidly advancing non-invasive devices, while achieving both an ultra-low detection limit and wide sensing range concurrently presents a challenge. Herein, we propose a liquid metal (LM) strain sensors manufacturing strategy employing aerosol jet printing (AJP). Specially formulated LM ink is the key to enabling high-precision printing (12 μm) of LM via AJP, which is optimized by adjusting the concentration of polyvinylpyrrolidone and diethylene glycol. Additionally, through structured sensor pattern design in conjunction with narrow line width AJP, flexible LM strain sensors are developed that feature an ultralow detection limit (0.1% for I-sinusoid and 0.0033% for s wave LM strain sensors) combined with a wide sensing range (660% for I-sinusoid and 230% for s wave). Exceptional performance achieves comprehensive detection of human movement. This research reconciles the trade-off between detection limit and sensing range, while high-precision LM Aerosol-jet Micro-patterning enhances manufacturing in flexible electronics.

Wearable resistive flexible strain sensors (FSS) are non-invasive soft electronic devices that effectively convert biological signals from the human body into electrical signals^{1–3}. Recently, these sensors have gained significant attention and application in areas such as health monitoring⁴, motion detection^{5,6}, and human-machine interfaces⁷. An ideal FSS should possess low minimum detection limit ($\varepsilon_{\text{emin}}$) and a wide sensing range ($\varepsilon_{\text{emax}}$) to monitor full-range human motion that accurately captures subtle physiological signals (e.g., pulse with strain <1%) as well as large joint movements (e.g., knee flexion with strain >100%)^{8–12}. However, lower $\varepsilon_{\text{emin}}$ typically necessitate a significantly reduction in the conductive network during minor strain changes, whereas a wider $\varepsilon_{\text{emax}}$ demands a stable conductive pathway under large strains^{9,11,13}. So, achieving ultra-low $\varepsilon_{\text{emin}}$ while maintaining wide $\varepsilon_{\text{emax}}$ poses a considerable challenge.

Recent studies indicate that, unlike rigid metals (e.g., silver^{14–16}, gold¹⁷) and carbon-based materials (e.g., carbon nanotubes^{11–13,18,19}, graphene^{20–22}, carbon black¹⁰), biocompatible gallium-based room-

temperature liquid metals (LM, such as EGaIn) demonstrate exceptional performance in large-strain sensing due to their unique flow properties^{23–25}. LM maintain excellent conductivity even under extreme tensile conditions, effectively aligning with the elastic interfacial modulus^{26,27}. However, this characteristic also makes it a challenge for LM to sense minor strains. Currently, a common approach to address this limitation involves integrating other materials (e.g., graphene⁹, SiO_2 ²⁸) into the LM, which creates micro-cracks during minor strains, thus lowering the $\varepsilon_{\text{emin}}$, while the propagation of micro-cracks limits $\varepsilon_{\text{emax}}$. Another approach involves carefully designing the line width and shape of sensor patterns to correspond to strain distribution, thereby enhancing the sensing performance of liquid metal strain sensors (LMSS)^{29–33}. Hence, high-precision patterning methods for LM are anticipated to enable LMSS to simultaneously achieve ultra-low $\varepsilon_{\text{emin}}$ and exceptionally wide $\varepsilon_{\text{emax}}$.

In recent years, researchers have proposed various methods for patterning LM, including injection molding³⁰, mask printing^{9,34}, surface

¹State Key Laboratory of Clean and Efficient Turbomachinery Power Equipment, Department of Mechanical Engineering, Tsinghua University, Beijing, China.

²Key Laboratory for Advanced Materials Processing Technology, Ministry of Education, Beijing, China. ✉ e-mail: zhouming@tsinghua.edu.cn

modification^{35–37}, and direct writing technology (DWT)³⁸. Among them, DWT offers notable advantages by avoiding the high cost, material waste, and complexity associated with other techniques³⁹. DWT adjusts the rheological properties and enhancing wetting properties of LM²³, which are essential for effective LM patterning, by incorporating elastomers (e.g., Ecoflex²⁷), polymers (e.g., poly(vinyl alcohol)³⁸), metal powders (e.g., Ni⁴⁰), or by dispersing LM in a solvent to create liquid metal ink (LMI)^{41,42}. Nevertheless, the precision of DWT is generally limited to over 100 μm . Aerosol Jet Printing (AJP) is a high precision (10–200 μm) DWT that deposits atomized functional inks onto substrates using gas focusing^{43,44}. Although the ink viscosity is required to be less than 5 mPa·s, AJP with ultrasonic atomizer is preferred due to simpler in structure and higher printing precision⁴³. Researchers have developed various ink systems (e.g., silver¹⁴, graphene⁴⁵, and benzocyclobutene⁴⁶), allowing AJP to fabricate a wide range of functional devices. However, the absence of systematic ink design limits AJP's broader use. Pure LM and existing LMIs are too viscous for ultrasonic, causing premature drying and poor printing even after successful atomization^{47,48}. Therefore, there is an urgent need to develop novel LMI suitable for AJP, enabling the fabrication of meticulously designed high-precision LM patterns for exploring both ultra-low $\varepsilon_{\text{emin}}$ and wide $\varepsilon_{\text{emax}}$ in LMSS.

In this work, we have developed a strategy to regulate the dispersibility, viscosity, wettability, and volatility of LMI by adjusting the concentration of polyvinylpyrrolidone (PVP) and diethylene glycol (DEG) to meet the requirements of each step in the AJP process. Low viscosity facilitated fine aerosol generation, while controlled volatility suppressed overspray and ensured clean patterning. The optimized ink enabled high-precision (12 μm) patterning on various substrates via AJP. As a result, AJP-printed LM patterns on flexible substrates exhibited excellent strain-sensing performance. Reducing the pattern line width improved strain sensitivity, leading to a lower detection limit, and enabled complex structures in a limited area, where stress concentration enhanced sensitivity and stress dispersion broadened the sensing range. By employing AJP to fabricate structured sensor patterns with minimal line widths, we successfully developed LMSS with both ultra-low $\varepsilon_{\text{emin}}$ and wide $\varepsilon_{\text{emax}}$: l-sinusoid (0.1%–660%, 30 μm –198 mm), s wave (0.0033%–230%, 1 μm –69 mm), and 60 μm linear (0.0067%–360%, 2 μm –108 mm). In practical applications, beyond detecting significant joint movements and subtle facial expressions, the high-performance LMSS can also capture physiological signals. The manufacturing method and sensor design strategies proposed in this paper provide new insights for the rapid development of AJP inks, and the precise fabrication of meticulously designed LMI patterns using AJP has significantly advanced the development of high-performance wearable strain sensors with ultra-low $\varepsilon_{\text{emin}}$ and exceptionally wide $\varepsilon_{\text{emax}}$.

Results

Overall strategy

Figure 1a illustrates the AJP equipment and process, which could freely deposit LMI patterns on various substrates. Firstly, the LM was dispersed into a low-viscosity, well-dispersed nano ink by ultrasonic fragmentation in an ethanol-based solution containing PVP, ensuring good atomization. To reduce the volatility of ink and suppress overspray for clean patterning, a high-boiling-point solvent, DEG, was added. Subsequently, the LMI was aerosolized using a microporous ultrasonic atomizer, and then the aerosol was then focused into a micro-stream by gas and precisely deposited onto various substrates via a printhead, followed by drying to fix the LMI patterns. To enable successful AJP, a formulation strategy was developed to regulate the dispersibility, viscosity, wettability, and volatility of LMI, meeting the specific requirements of each step in the process. Using a self-built AJP prototype (Fig. S1), we successfully printed various LMI micro-patterns (Fig. 1b) on commonly used substrates. These included: (i) rigid substrates such as glass slides and silicon wafers; (ii) flexible substrates

including paper, polyimide (PI) films, and plant leaves; (iii) stretchable substrates such as nitrile gloves, polydimethylsiloxane (PDMS) films, and 3M tapes. By optimizing ink composition and AJP process parameters, we achieved the finest LMI lines of 12 μm on glass slides (Fig. S2).

After drying on a stretchable substrate and subsequent mechanical activation, the LMI patterns could be employed as strain sensors for monitoring human motion. The effects of line width and pattern geometry on sensor performance were further investigated. Reduced line widths improved sensitivity and lowered the detection limit, while complex patterns modified stress distribution to enhance both sensitivity and sensing range. Through structured sensing pattern design and AJP printing with small line width, the LMSSs are produced with ultra-low minimum detection limit and ultra-wide sensing range, thereby achieving a high sensing range-to-detection limit ratio ($\varepsilon_{\text{emax}}/\varepsilon_{\text{emin}}$) that demonstrated superior performance compared to other strain sensors (Figs. 1c and S3; Table S1).

Ink physical and chemical properties optimization

Achieving stable ink atomization is the first step toward ensuring reliable AJP printing. While microporous ultrasonic atomizers can effectively aerosolize suspensions, ink sedimentation and stratification within a short period can interrupt atomization⁴⁹. Therefore, it is essential to prepare stable inks with good dispersion properties. The sedimentation rate of particles in a suspension under gravity follows Stokes' law:

$$v = \frac{2r^2(\rho_1 - \rho_2)g}{9\eta} \quad (1)$$

where v represents the sedimentation velocity, r is the particle radius, ρ_1 and ρ_2 are the densities of the particles and the medium, respectively, g is the gravitational acceleration, and η is the viscosity of the dispersing medium⁵⁰. A smaller sedimentation rate of the suspension particles indicates better dynamic stability. According to Eq. 1, the stability of the suspension can be enhanced by reducing the particle radius and adding dispersants.

Based on previous literature^{42,51,52}, we prepared stable liquid metal ink (LMI) by using an ultrasonic shear method and adding PVP. As shown in Fig. 2a, ultrasonic treatment in the PVP ethanol solution resulted in smaller spherical particles with a narrower size distribution (micrometer to sub-micrometer range) compared with treatment without PVP (Fig. S4). Specifically, increasing the ultrasonic treatment time led to a reduction in the average particle size of LM (Figs. 2b and S5). After 2 h of ultrasonic treatment, the average particle size was reduced to less than 450 nm. Here, we named the inks, which had been prepared with 2 h ultrasonic treatment and added DEG to regulate its evaporation rate, from LMI@OP to LMI@30P based on the concentration of PVP. However, the average particle size of LMI first decreased and then increased with higher PVP concentrations. Due to the formation of an excessively thick PVP layer on the LM particle surface, which hinders further breakdown. LMI@10P achieved the smallest average particle size of 291 nm. Subsequently, we quantitatively investigated the time stability of LMI by measuring the relative absorption of visible light (Fig. 2c). The LMI without PVP (LMI@OP) was started to stratify after 46 min, with complete sedimentation of LM particles after 2.2 h, leaving the supernatant colorless and transparent. In contrast, stability of LMI improved with increasing PVP concentration. When the concentration of PVP reaches 10 mg/mL or higher, the LMI remained stable for up to 20 h. Although some stratification occurred after 20 h at a concentration of 10 mg/mL, the upper layer remained a light gray color. At a PVP concentration of 15 mg/mL or higher, the LMI achieved stability for as long as 35 h. This enhancement was attributed to the increased steric hindrance from PVP, which also raised the viscosity of the ink^{49,53}.

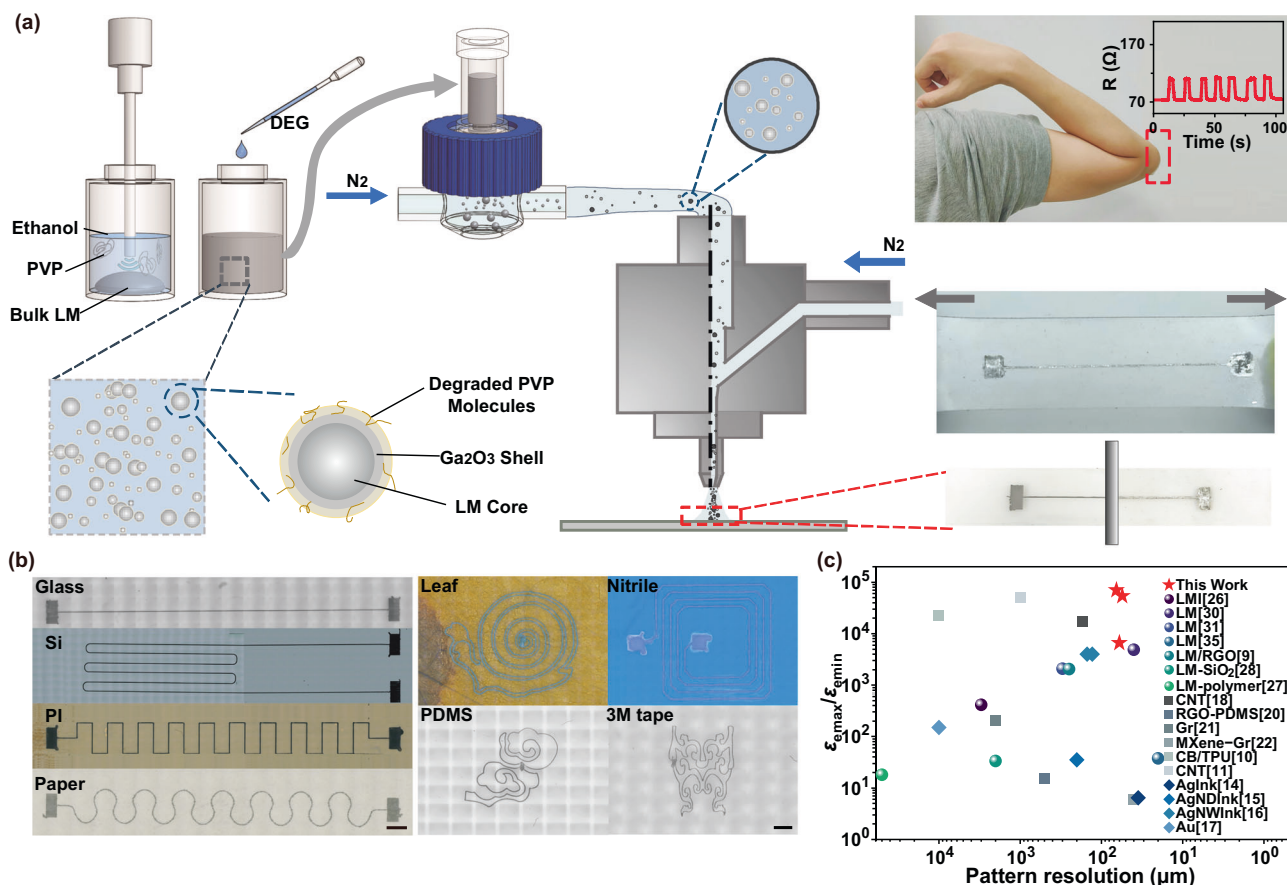


Fig. 1 | Illustration of the aerosol jet printing (AJP) strategy for liquid metal (LM) patterning and its application in high-performance flexible strain sensors. a Schematic of the overall AJP strategy for LM patterning and sensor fabrication. PVP and DEG denote polyvinylpyrrolidone and diethylene glycol, respectively. **b** AJP printing of LM patterns on various substrates, including glass slides, silicon wafers, polyimide (PI) films, paper, plant leaves, nitrile gloves,

polydimethylsiloxane (PDMS) films, and 3 M tapes (scale bar: 2 mm). The experiment was repeated independently three times with similar results. **c** Comparison of patterning resolution and the ratio of sensing range-to-detection limit ($\epsilon_{\text{max}}/\epsilon_{\text{min}}$) among various stretchable strain sensors. Source data are provided as a Source data file.

Hence, the rheological properties of the LMI were studied. Unlike EGaln, which exhibited shear-thinning behavior, LMI behaved as a Newtonian fluid (Fig. 2d). The viscosity of LMI increased linearly with PVP concentration (Fig. 2e). In addition, Fig. S6 shows that LMI has a higher storage modulus than loss modulus, reflecting an overall elastic behavior, while its overall modulus is lower than EGaln, facilitating ultrasonic nebulization. Combining the viscosity limit for ultrasonic atomization and ink stability, we selected five inks, LMI@10P to LMI@30P, for subsequent ultrasonic atomization studies. As the viscosity increased, the atomization amount of ink and the corresponding aerosol concentration decreased. The aerosols produced by the atomized LMI exhibited a polydisperse system ranging from 50 nm to 2.5 μm (Fig. S7). Notably, the increase in ink viscosity had little effect on the aerosol drop size (Fig. 2g). The average number size of aerosols from different viscosity inks was $\sim 1.00 \mu\text{m}$, about three times than the average ink particle size. The mass mean size of aerosols was about 1.33 μm , indicating that ink viscosity has minimal impact on the aerodynamic behavior of the aerosols. In summary, LMI@10P–LMI@30P could achieve stable atomization using an ultrasonic atomizer in 20 h.

Additionally, while increasing PVP content slightly increased the surface tension of LMI, its maximum surface tension was only 4% of EGaln, and the surface tension of the ink was significantly reduced (Fig. 2h). Therefore, although the contact angle of LMI ink slightly increases with PVP concentration, the contact angle remained below 90° on typical substrates, such as glass slides and PDMS, indicating a

wettable state (Fig. 2i). This allowed LMI to be effectively deposited on various substrates, which was not achievable with EGaln.

Using the above measured average particle size, viscosity, and surface tension, theoretical sedimentation times to 10 mm (half the ink height and test position in Fig. 2c) were calculated via Stokes' law and compared with experimental values (Fig. S8). Stability increased with PVP, with deviations from aggregation (<10 mg/mL) and steric hindrance (>10 mg/mL).

Effect of ink physicochemical properties on AJP

Although the LMI prepared by ultrasonic fragmentation could be printed using AJP, it tended to clog the nozzle and produces lines with significant overspray, where the aerosol spread beyond the intended edges (Fig. 3a.i). This result was consistent with previous studies, which had shown that high-volatility solvents like ethanol evaporate, resulting in the deposition of dried particles when used alone, leading to pronounced overspray characteristics^{54,55}. It's demonstrated that the addition of $\sim 10\%$ v/v of a low-volatility cosolvent to the ink could prevent particle drying before deposition⁵⁶. DEG was selected as the second solvent due to its high boiling point, low viscosity, and surface tension. We investigated the effect of DEG concentrations on reducing ink overspray (Fig. 3a.ii–iv). As the concentration of DEG increases, the over-spraying phenomenon was progressively suppressed. When the DEG concentration reached 10%, the printed lines were smooth with no scatter. However, when the DEG concentration was increased to 15%, the line width enlarged, resulting in reduced printing accuracy.

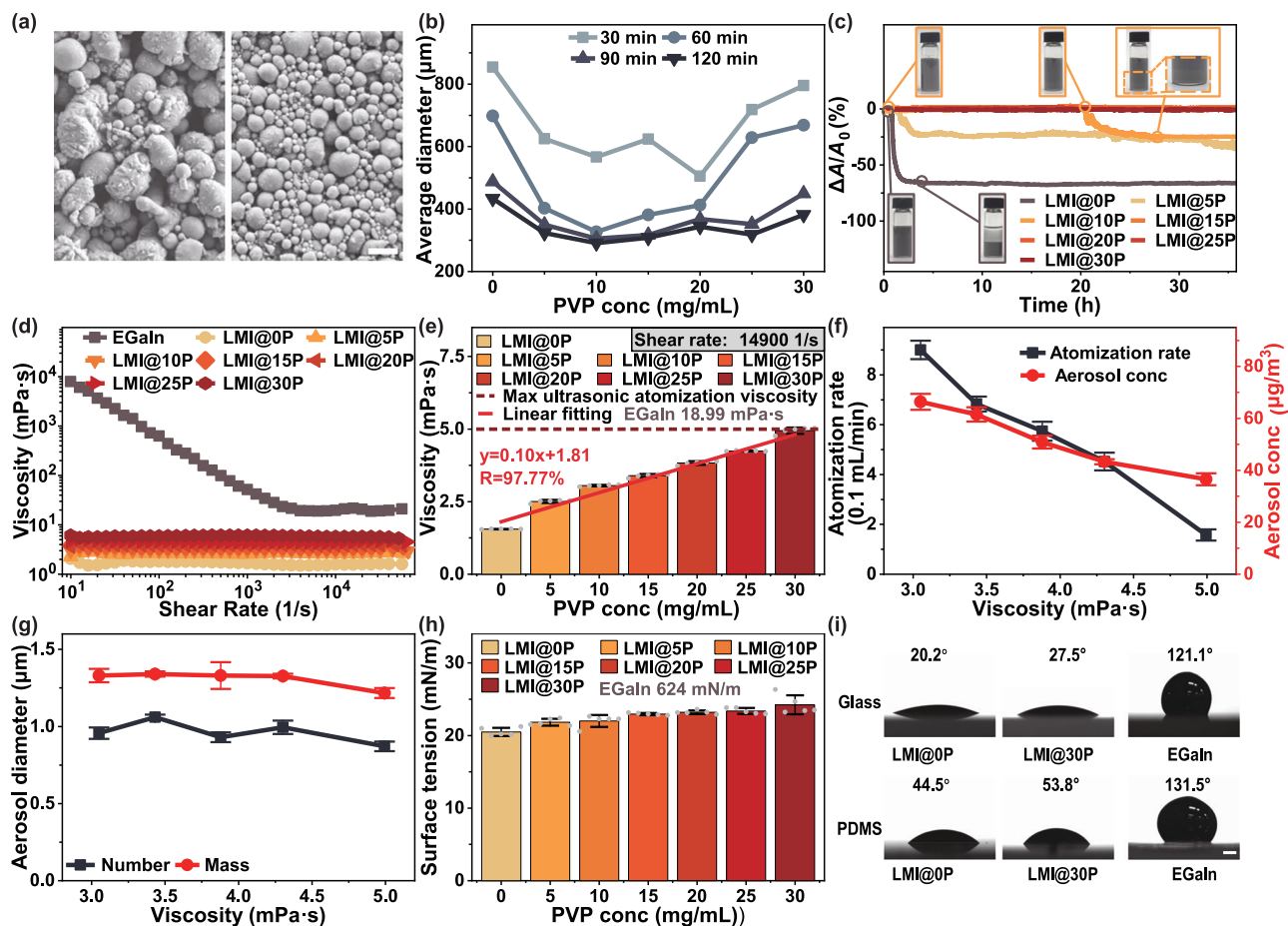


Fig. 2 | Optimization of physicochemical properties of ink by polyvinylpyrrolidone (PVP) concentration. **a** Scanning electron microscopy images of liquid metal ink (LMI) after 2 h of ultrasonic fragmentation in ethanol (left) and ethanol with 10 mg/mL PVP (right). Scale bar: 1 μm . The experiment was repeated independently three times with similar results. **b** Effect of PVP concentration (PVP conc) on the average particle size of LMI at different ultrasonic times. **c** Relative change in absorbance ($\Delta A/A_0$) of LMI as a function of time, with insets showing ink images at each time point. **d** Shear viscosity curves for EGaln and LMI. **e** Effect of PVP concentration on LMI viscosity. Bars show mean \pm SD; individual data points

($n = 5$) are overlaid. **f** Effect of LMI viscosity on ultrasonic atomization rate and aerosol concentration. Data are presented as mean \pm SD ($n = 3$ independent replicates). **g** Effect of LMI viscosity on aerosol particle size. Data are presented as mean \pm SD ($n = 3$ independent replicates). **h** Effect of PVP concentration on LMI surface tension. Bars show mean \pm SD; individual data points ($n = 5$) are overlaid. **i** Contact angles of LMI and EGaln on glass slides and PDMS. The experiment was repeated independently three times with similar results. Scale bar: 500 μm . Source data are provided as a Source data file.

Because there was too high DEG concentration of LMI to dry timely, leading to excessive spread on the substrate. Therefore, a DEG concentration of 10% v/v was selected as the optimal formulation to completely suppress overspray while maintaining the highest printing precision.

As known, the collision dynamics between the droplet and the substrate critically determine the printing accuracy and quality for inkjet printing⁵⁷. The spreading behavior of droplets upon impact with a substrate had been studied in depth⁵⁸. The maximum spreading area achieved after droplet impact is closely related to printing precision. Typically, the degree of maximum spreading on the substrate is described by the maximum spreading coefficient, $\beta_{\text{max}} = r_{\text{max}}/r_0$, where r_0 is the initial droplet radius and r_{max} is the maximum spreading radius of the droplet upon impact. The droplet spreading process is primarily governed by inertia, capillary forces, and viscous forces, described using two dimensionless parameters: the Weber number (We) and the Reynolds number (Re). AJP is a process characterized by low viscosity and high We , conforming to the general formula proposed by Lann et al.

$$\beta_{\text{max}} Re^{-\frac{1}{5}} = P^{\frac{1}{2}} / (A + P^{\frac{1}{2}}) \quad (2)$$

where $P = We Re^{-2/5}$, means impact number, and $A = 1.24 \pm 0.01$, serves as a fitting coefficient⁵⁹.

In the section “Ink physical and chemical properties optimization”, we observed that increasing the concentration of PVP led to higher ink viscosity and surface tension. This increase was likely to suppress the spreading of aerosol ink droplets upon impact, thereby improving printing precision. So, we conducted AJP experiments. The 3D profile of the printed LMI lines is shown in Fig. 3b, while the line width (Lw) was measured using the cross-sectional image (Fig. 3c) by identifying the height transition points relative to the substrate. The equivalent thickness was obtained by dividing the cross-sectional area by the line width. In agreement with the theoretical formula for the maximum spreading diameter (D_{max}) of droplets (Fig. 3d), we found that Lw decreased as the ink viscosity increased (Figs. 3e and S9). It is important to note that, unlike predictions based solely on single droplet impact, Lw decreased with the increase of sheath gas flow rate. This phenomenon occurs because AJP is a multi-droplet deposition process. Although higher sheath gas flow rates increase droplet velocity, which would theoretically enlarge D_{max} and Lw , they also enhance the convergence of aerosol droplets, which in turn reduced Lw . Therefore, in AJP, the convergence of multiple droplets plays a more significant role in determining Lw than droplet impact velocity. To

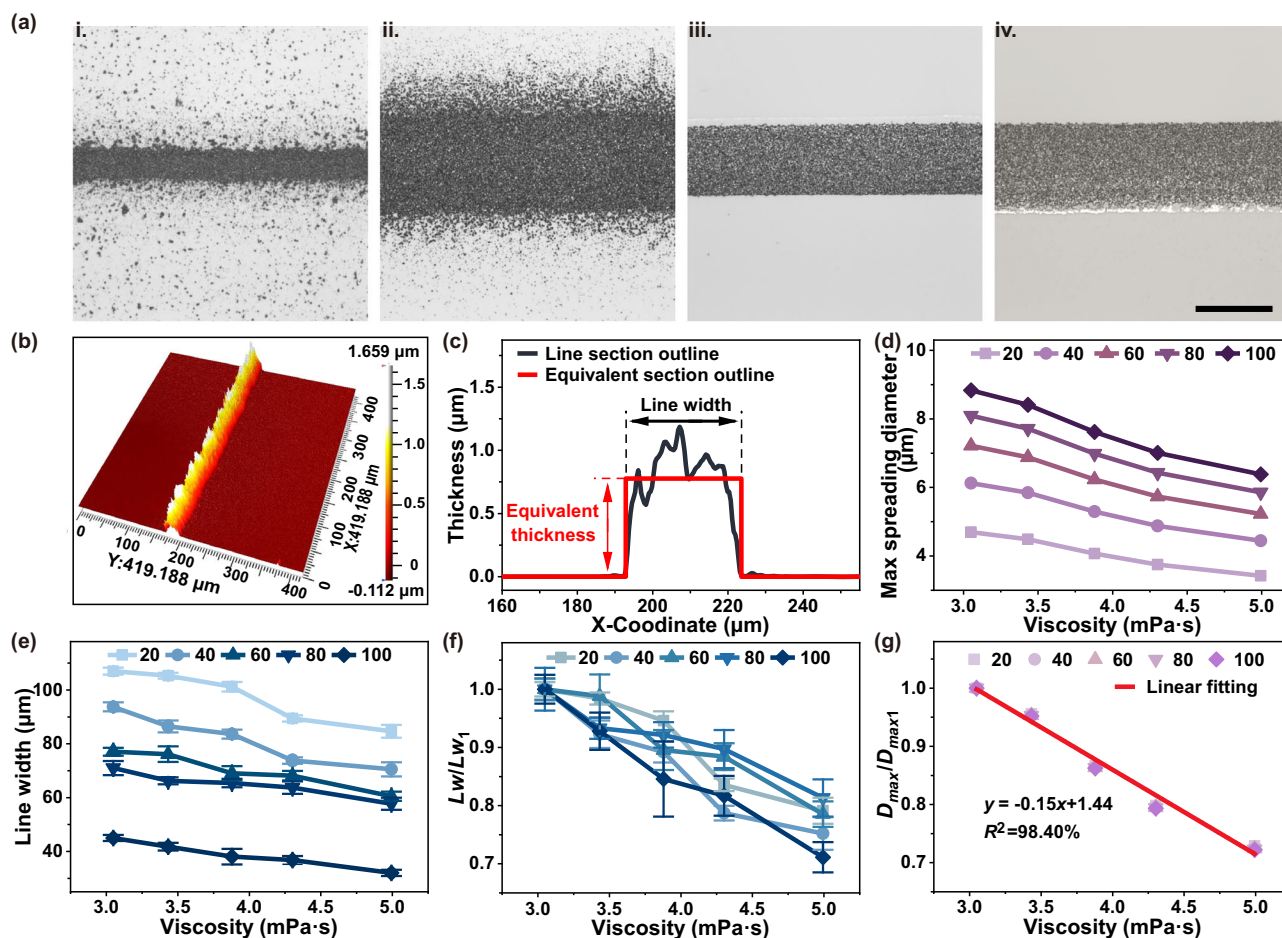


Fig. 3 | Regulation of printing performance by ink properties. **a** Optical microscopy images of lines printed via aerosol jet printing (AJP) at a sheath gas flow rate of 60 sccm with diethylene glycol (DEG) concentrations of i. 0% v/v, ii. 5% v/v, iii. 10% v/v, and iv. 15% v/v. Scale bar: 100 μm . The experiment was repeated independently three times with similar results. **b** 3D view and **c** cross-sectional view of liquid metal ink (LMI@30P, LMI with 30 mg/mL PVP) lines printed via AJP at a sheath gas flow rate of 100 sccm. **d** Variation of the calculated maximum spreading diameter with LMI viscosity at different sheath gas flow rates (sccm). **e** Variation of

the printed line width with viscosity at different sheath gas flow rates (sccm). Data are presented as mean values \pm SD ($n = 5$ independent replicates). **f** Normalized printed line width (Lw/Lw_1), where Lw_1 corresponds to that at 3.05 mPa·s, as a function of LMI viscosity at different sheath gas flow rates (sccm). Data are presented as mean values \pm SD ($n = 5$ independent replicates). **g** Normalized the calculated maximum spreading diameter (D_{max}/D_{max1}) as a function of ink viscosity at different sheath gas flow rates (sccm), where D_{max1} corresponds to 3.05 mPa·s. Source data are provided as a Source data file.

evaluate the influence of viscosity, we calculated the ratios of experimental Lw and theoretical D_{max} to their corresponding values at a viscosity of 3.05 mPa·s (Lw/Lw_1 , Fig. 3f, D_{max}/D_{max1} , Fig. 3g). At all flow rates, increasing the viscosity reduced both the line width and maximum spreading diameter to a similar degree. When viscosity was at its highest, the printed line width ranged from 71.13% to 81.31% of the baseline width, which aligned closely with theoretical predictions. Furthermore, we increased the printing speed to 13.5 mm/s, achieving continuous lines of LMI@30P with a minimum width of 12 μm (Fig. S10a, b). However, the excessively high printing speed resulted in discontinuities in the lines (Fig. S10c).

Based on the effects of ink physicochemical properties on AJP printing performance, we developed a systematic approach for preparing LMI, an insoluble AJP ink. The main steps include: (1) generating nanoscale LM particles via top-down ultrasonic fragmentation; (2) adding surfactants to improve the stability of LM ink; and (3) introducing a non-volatile solvent as a second solvent to optimize evaporation properties. Key to stable atomization and reliable AJP printing is reducing LM particle size, selecting appropriate solvents, and incorporating effective surfactants to achieve a stable functional ink. Remains within atomization limits, increasing viscosity further

enhances printing precision by minimizing droplet impact spreading. In addition, this strategy also serves as a general framework for solute–solvent aerosol ink formulation. To meet functional requirements like conductivity, magnetism, and hardness, low-viscosity AJP inks based on carbon nanotubes (CNTs), graphene, Fe, and SiC were developed. As shown in Fig. S11, these inks yielded clean, splatter-free patterns, demonstrating the versatility and rapid adaptability of this approach for next-generation high-resolution, flexible electronic fabrication.

Electromechanical performance of LM pattern

After drying, the LMI pattern consisted of a stack of LM particles (Fig. 4a, left), which was non-conductive. To activate the electrical conductivity of the LM pattern, the oxide layer encapsulating the LM particles must be disrupted, causing the inside LM to overflow and connect to form a continuous conductive film. We achieved this by rolling an iron rod over the pattern. After rolling, the pattern transformed into a continuous LM film (Fig. 4a, right) with activated conductivity. The conductivity of the activated LMI pattern decreased as the PVP concentration increased (Fig. 4b). Because a higher PVP concentration resulted in a thicker insulating layer on the surface of LM

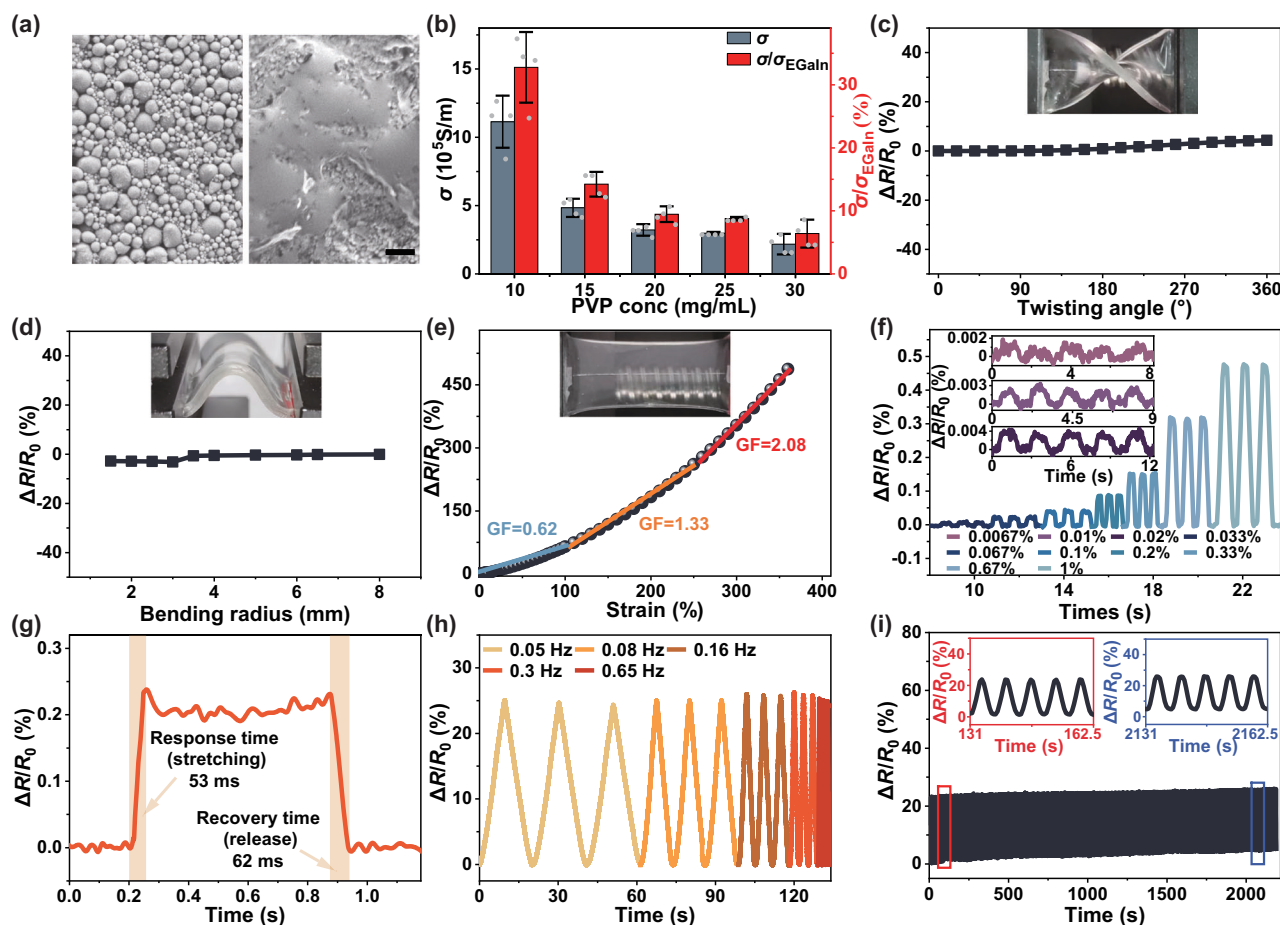


Fig. 4 | Electrical properties of liquid metal (LM) pattern printed via aerosol jet printing (AJP). **a** SEM images of printed patterns before (left) and after (right) compression using an iron rod (scale bar: 1 μm). The experiment was repeated independently three times with similar results. **b** The effect of polyvinylpyrrolidone (PVP) concentration (PVP conc) on the conductivity (σ) and relative conductivity ($\sigma/\sigma_{\text{EGain}}$) of activated LM. Bars show mean \pm SD, and individual data points ($n = 4$) are overlaid. Relative change in resistance ($\Delta R/R_0$) of activated LM ink (LMI) line

under **c** twisting, **d** bending, and **e** stretching, with insets showing photographs of the corresponding deformations. The gauge factor (GF) was extracted from the slope of a linear fit. **f** Cyclic signals under subtle strain. **g** Response and recovery times under 0.5% tensile strain. **h** Cyclic signals at stretch rates of 1.5–19.5 mm/s (0.05–0.65 Hz) under 50% tensile strain. **i** $\Delta R/R_0$ during 350 cycles of 50% strain, with insets showing magnified signals from 5 stretching cycles in the periods of 209–241 s and 2540–2577 s. Source data are provided as a Source data file.

particles, which became more difficult to break, reducing the proportion of activated. Moreover, as the insulating layer broke, the increased concentration of PVP in the LMI pattern further reduced overall conductivity. To balance printing precision and electrical performance, we selected LMI@15P as the optimal ink for subsequent experiments, achieving a conductivity of $4.84 \times 10^5 \text{ S/m}$. However, during the activation of LMI patterns printed on stretchable substrates, the deformation of the substrate during rolling increased the difficulty of activation. A 30 mm LMI line printed on stretchable 3M tape, when activated by rolling, exhibited a resistance of up to 1.09 k Ω . Increasing the number of print passes enlarged the cross-sectional area of the printed lines, improving conductivity (Fig. S12). After 9 print passes, the resistance of the LMI line decreased to 73.64 Ω , with a line width of 60 μm . To ensure optimal conductivity after LMI activation, we selected LMI lines printed in 9 passes for further study.

The LMI line printed and activated on 3M tape exhibited excellent stretchability and electrical performance, making it suitable for use as wearable sensors. To evaluate the sensing performance of the LMI line, we measured its relative change in resistance ($\Delta R/R_0$) under twisting (Fig. 4c), bending (Fig. 4d), and stretching (Fig. 4e). Under twisting and bending $\Delta R/R_0$ was minimal, with resistance remaining largely stable (Fig. 4c, d). When stretching, $\Delta R/R_0$ increased monotonically with strain, demonstrating a clear strain-responsive behavior

(Fig. 4e). Based on sensing curve, three distinct linear regions with different slopes were observed within the 0–360% strain range. In the 0–100% strain range, the gauge factor (GF) was 0.62, which was slope by linear fitting. In the 100–250% strain range, the GF was 1.33. And in the 250–360% strain range, the GF was 2.08. However, when the strain was increased beyond 370%, the LM line lost conductivity. Notably, during repeated micro-strain from 0.0067% to 1%, identifiable resistance changes were observed in the LM line (Fig. 4f), with a GF of 0.48 (Fig. S13). The minimum detectable deformation limit was as low as 2 μm (0.0067% strain), surpassing most flexible strain sensors (Fig. 1c, Table S1). Overall, the LMI line provided consistent and unique signals across a strain range of 0.0067–360%, which held significant potential for practical applications as strain sensors.

A rapid response time is also a key requirement for an ideal strain sensor. When stretched at a rate of 2.9 mm/s, the LMI line exhibited a response time of 53 ms to reach 0.5% strain, while 62 ms to return, showing a 9 ms delay in the recovery phase compared to the stretching phase (Fig. 4g). This hysteresis is commonly observed in flexible strain sensors due to the residual stress persists between polymer substrate and the sensing material after the external force is removed^{24,60–62}. Subsequently, at 50% strain, the LMI line produced stable sensing signals across a range of stretching rates from 1.5 mm/s to 19.5 mm/s, with minimal changes in the signal waveform (Fig. 4h). Therefore, the

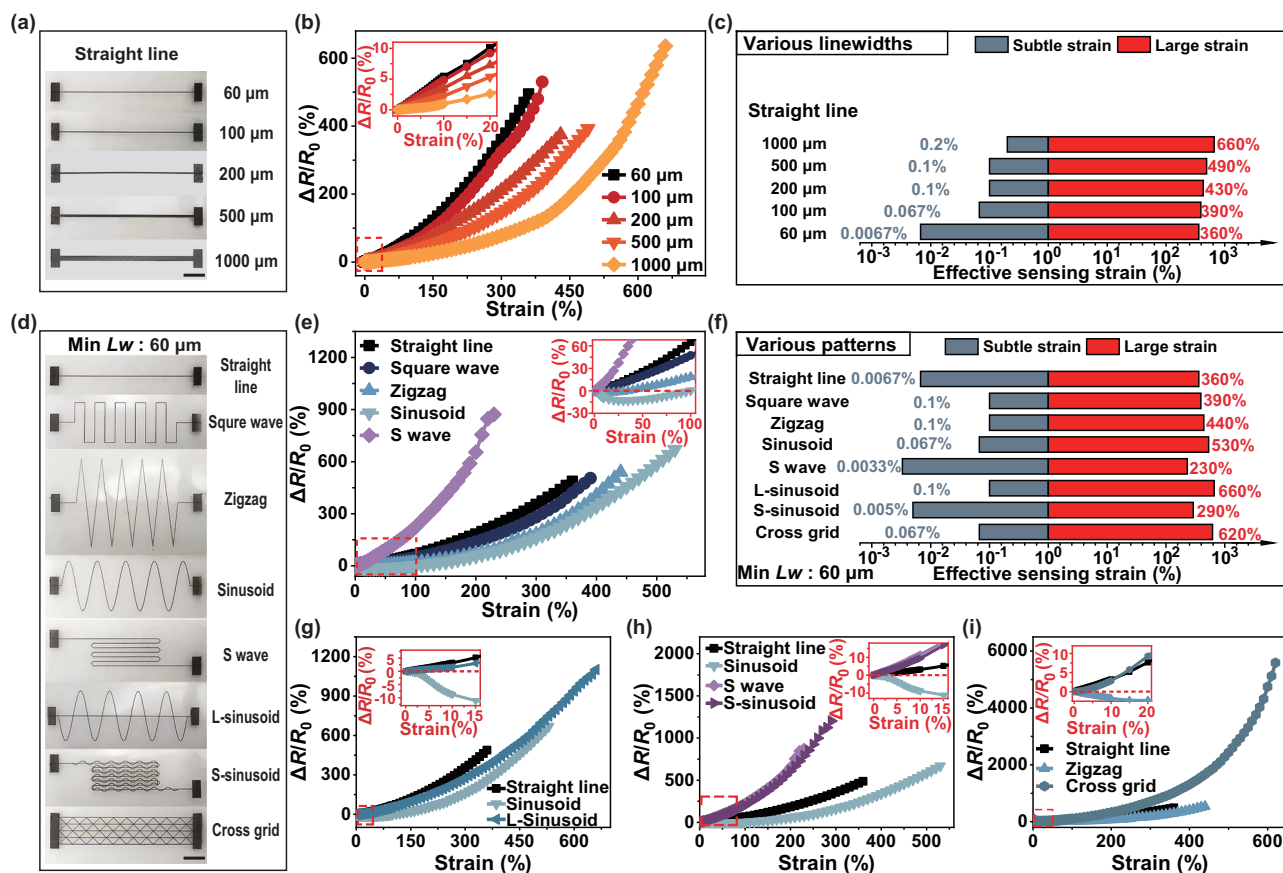


Fig. 5 | The effect of varying line widths and patterns on the performance of liquid metal strain sensors (LMSS). **a** Optical images of LMSS with different line widths printed using aerosol jet printing (AJP) (scale bar: 5 mm). The experiment was repeated independently three times with similar results. **b** Sensing response curves of straight LMSS with varying line widths. **c** Influence of line width on the effective sensing strain of LMSS. **d** Optical images of AJP-printed LMSS with different patterns, featuring a minimum line width (min Lw) of 60 μm (scale bar: 5 mm). The experiment was repeated independently three times with similar results. **e** Sensing response curves of LMSS with five basic shapes, with insets showing magnified views. **f** The influence of patterns on the effective sensing strain of LMSS. Composite patterns: **g** L-sinusoid, **h** S-sinusoid, and **i** cross-grid, compared with the response curves of their corresponding basic shapes, with insets showing magnified views. Source data are provided as a Source data file.

strain sensing behavior is independent of the stretching rate, which is beneficial for the accurate and stable detection of human motion. Reproducibility and stability during long-term stretching and releasing cycles are essential for flexible strain sensors. We evaluated the strain sensing performance of the LMI line over 350 cycles at 50% strain (Fig. 4i). The sensor maintained stable performance throughout the stretching cycles. Although the $\Delta R/R_0$ increased slightly with the number of cycles, the rate of increase slowed as the cycles progressed. Magnified views of the sensing response at the beginning and end of the cycles showed that the $\Delta R/R_0$ followed a consistent periodic pattern, with the peak values and waveform remaining almost unchanged, indicating good stability and durability. Finally, we tested the current-voltage (I-V) characteristics of the LMI line under different strain levels (Fig. S14). The I-V curves were linear at all strain levels, indicating ohmic behavior. As strain increased, the slope of the I-V curves decreased, reflecting an increase in the sensor's resistance.

Influence of precision and pattern on sensing performance

The theoretical model for the intrinsic stretchable strain sensor is based on the change of resistance caused by deformation^{29,32}. Two strain loading conditions is considered: longitudinal and transverse stretching along the pattern, referred as longitudinal and transverse condition, respectively (Fig. S15a)⁶³. By analyzing the changes in the cross-sectional area and length of the LM line, the dependence of

$\Delta R/R_0$ on the applied strain (ϵ) can be determined (for the detailed derivations, see Note S1). The expression for this dependence is given by:

Longitudinal condition:

$$\frac{\Delta R_{ex}}{R_0} = \lambda_x (1 + \epsilon_x)^2 - 1 \quad (3)$$

Transverse condition:

$$\frac{\Delta R_{ey}}{R_0} = \lambda_y (1 - \nu_{xy} \epsilon_y)^2 - 1 \quad (4)$$

where ϵ_x and ϵ_y are the stretching strain under longitudinal and transverse stretching, $\Delta R_{ex}/R_0$ and $\Delta R_{ey}/R_0$ are the relative resistance of stretched LM line, λ_x and λ_y are the shape factor for irregular deformation of LM line with elastic substrates respectively⁶⁴, while ν_{yz} represents the Poisson's ratio during transverse stretching. Under ideal or upstretched conditions, $\lambda_x = \lambda_y = 1$. For LM, which is an incompressible fluid, the Poisson's ratio is 0.5. By applying Eqs. (3) and (4), sensing curves for longitudinal and transverse stretching were plotted (Fig. S15b). Interestingly, when the strain is below 400%, $\Delta R/R_0$ becomes negative, which is called as "negative value segment" (Table S3). It was important to note that the negative value segment

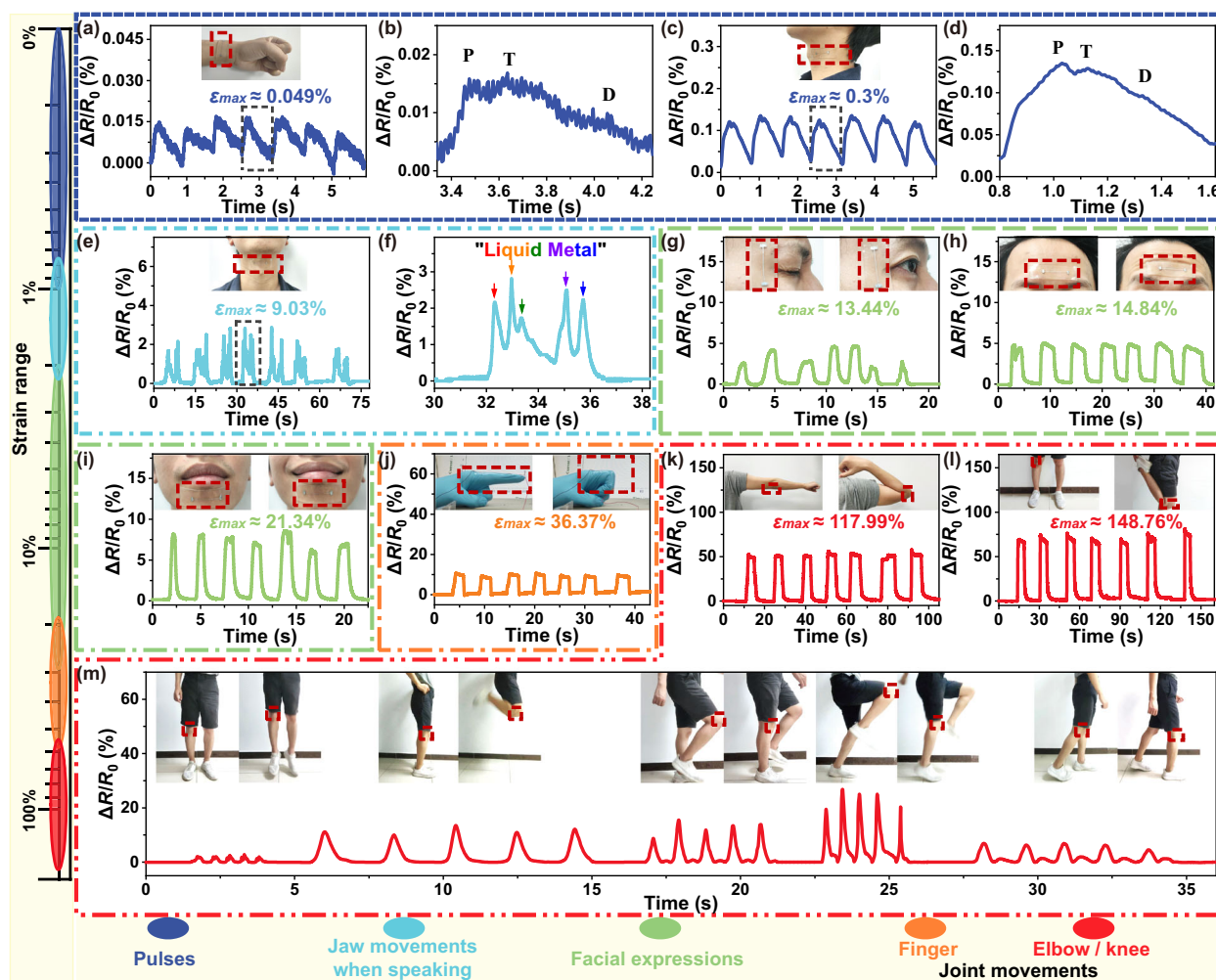


Fig. 6 | Liquid metal strain sensors (LMSS) for human motion detection. Physiological signal monitoring: **a** resistance signals ($\Delta R/R_0$) of radial artery pulses with the maximum strain (ϵ_{max}) estimated from the sensing characteristic curve. **b** Magnified view of a single pulse from (a), with three characteristic peaks identified as the percussion wave (P), tidal wave (T), and diastolic wave (D). **c** Carotid artery pulses, and **d** magnified view of a single resistance pulse from (c). Vocal vibration monitoring: **e** resistance signal during the pronunciation of “Liquid Metal”

and **f** magnified view of the resistance signal from a single pronunciation. Facial micro-expression monitoring: **g** blinking, **h** eyebrow raising, and **i** smiling. Joint bending monitoring: **j** index finger bending, **k** elbow flexion, and **l** knee flexion. Physical activity monitoring: **m** jumping in place, knee-bend jumping, marching in place, high-knee running in place, and walking. Insets show photographs of the strain sensor attached to various locations on the human body. Source data are provided as a Source data file.

was not monotonic, and the $\Delta R/R_0$ did not correspond linearly with strain in this phase. This characteristic hindered its potential application as a strain sensor, making it essential to minimize the presence of the negative value segment. The negative value segment was caused that at low transverse strain ($\epsilon < 200\%$), the sensor's length decreases while its cross-sectional area remains nearly constant, resulting in a reduction of resistance. With further stretching, the reduction in cross-sectional area surpasses the length contraction, leading to an increase in resistance. Throughout the process, $\Delta R/R_0$ and sensitivity for transverse stretching are consistently lower than for longitudinal stretching. When a $60\ \mu\text{m}$ LMSS was stretched longitudinally and transversely, the obtained sensor response curves followed the general trend predicted by the equations, though the specific values varied due to the influence of the shape factor (Fig. S16a). During transversely stretching, the segment of negative growth in $\Delta R/R_0$ occurred when the strain is less than 10% (Table S3). The non-monotonic negative value segment was observed when the strain is less than 25%. In addition, the ϵ_{min} for transverse stretching was 0.2%, an order of magnitude higher than longitudinal stretching, resulting in a loss of

detection capability for subtle strains in the 0.0067% to 0.2% range (Fig. S16b). However, the ϵ_{max} for transverse stretching reached 520%, which is 1.44 times that of longitudinal stretching. Therefore, sensor performance can be tuned by adjusting the shape factor through pattern design and distributing strain across the transverse direction.

We employed AJP to print a series of strain sensors with varying line widths (Fig. 5a) and patterns (Fig. 5d) to investigate the effects of manufacturing precision and pattern design on the ϵ_{max} and ϵ_{min} of LMSS. We fabricated five sets of straight-line sensors with different line widths, each having a length of 30 mm (Fig. 5a). While maintaining consistent length and equivalent thickness (Fig. S17), varying the line width alters the pattern's anisotropy and shape factor, resulting in different sensing responses. All five sensors demonstrated a good response with strain, with $\Delta R/R_0$ increasing as strain increased. As the line width increased, the rate of increase $\Delta R/R_0$ slowed (Fig. 5b, Table S2), leading to a larger ϵ_{max} . The sensor with a 1 mm line width achieved a ϵ_{max} of 660%. However, the sensitivity to subtle strains decreased with increasing line width (Fig. S18), resulting in a higher ϵ_{min} (Fig. 5c, Table S2). The 1 mm sensor can only detect strains as low

as 0.15%, two orders of magnitude higher than the 60 μm sensor. While line width adjustments can regulate the ε_{max} and ε_{min} , they do not allow for the simultaneous optimization of both. Consequently, we chose the 60 μm line width as the baseline for further exploration of patterning effects on sensing performance.

We designed eight distinct patterns (Fig. 5d), with the first five being basic patterns and the last three being composite patterns. In addition to the linear pattern, the other four basic patterns had same length (120 mm). During stretching, $\Delta R/R_0$ of the s wave, straight line, square wave, zigzag wave, and sinusoidal wave decreased sequentially (Fig. 5e). The corresponding ε_{max} increased sequentially, with the ε_{min} increasing in the order of s wave, straight line, sinusoidal wave, square wave, and zigzag wave (Figs. 5f and S19, Table S2). One hand, this trend was attributed to the fact that the s wave, compared to the straight line, increased the longitudinal length and concentrates more strain, thereby enhancing sensitivity and enabling detection of smaller strains. The s wave LMSS exhibited a minimum ε_{min} of 0.0033%, which is lower than that of the straight line. While this concentrated strain can accelerate crack formation, leading to sensor failure and reducing the ε_{max} . On the other hand, the structures of the square wave, zigzag wave, and sinusoidal wave progressively straighten, effectively absorbing strain during stretching. Thus, the increased transverse length reduced sensitivity, causing a loss of response to certain subtle strains, and simultaneously delays sensor failure, enlarging the ε_{max} . The smoothness of the square wave, zigzag wave, and sinusoidal wave structures increased sequentially, which allowed them to absorb greater strain and results in a corresponding increase in their ε_{max} . Although the ε_{min} decreased in the same order, the non-monotonic negative value segment became larger (Tables S2 and S3), making these structures less suitable for using as strain sensors.

Furthermore, we designed three composite patterns, each exhibiting monotonic increasing sensor curves, as illustrated in Fig. 5g–i. Specifically, the l-sinusoid pattern, which combined a straight line with a sinusoidal wave, showed a sensor curve that lied between those of the straight line and sinusoidal wave (Fig. 5g). Although the ε_{min} increased to 0.1% (see Fig. S20a) compared to the linear and sinusoidal patterns, this configuration also significantly enhanced the ε_{max} by 660%. The s-sinusoid pattern merged an s wave with a sinusoidal wave, offering sensitivity between the two (Fig. 5h). It maintained a ε_{min} of 0.005% (Fig. S20b, c) and increased the ε_{max} to 290%, meaning that s-sinusoid LMSS retained the s wave's capability for detecting minute strains and significant improved sensing ability to large strains. The cross-grid pattern, which combined multiple straight lines with a triangular wave, had lower sensitivity than the straight line at strains below 6% (Fig. 5i). Its ε_{min} is 0.067% (Fig. S20d), which is bigger than the straight line but slightly less than the triangular wave. At higher strains, its sensitivity surpasses both the straight line and the triangular wave, interestingly providing a higher ε_{max} (620%) than either. The performance of composite pattern LMSS is usually between that of basic pattern LMSS, which is essentially because the composite sensing pattern is obtained in parallel with the basic patterns. At low strains, the $\Delta R/R_0$ of composite pattern LMSS is more similar to that of stress-concentrated basic patterns like the straight line and s wave, while at high strains, it resembles stress-dispersed patterns such as the sinusoidal wave and zigzag wave. By designing composite patterns with narrow line widths, such as the 60 μm cross-grid LMSS, the sensor achieves both a lower ε_{min} and a broader ε_{max} compared to the 500 μm straight-line LMSS, enabling a balanced optimization of ultra-low ε_{min} and ultra-wide ε_{max} . Aerosol printing, a high-precision patterning technology, facilitates the convenient fabrication of various LMI patterns, leading to enhanced performance in LMSS.

Application of LM wearable sensors

Based on its excellent performance, the 60 μm linear strain sensor was adhered to various locations on the body to evaluate its capability for

monitoring physiological signals and movement. Minor deformations in human signals, such as pulse and voice, are often crucial for health and information transmission. We attached the LMSS to the wrist, where it reliably recorded periodic pulsatile signals (Fig. 6a). From the pulse waveform, the single pulse duration was calculated to be 0.84 s, corresponding to a heart rate of 71.42 beats per minute, which fell within the normal range for a healthy individual. The amplified wrist pulse signal (Fig. 6b) showed distinct features of the arterial pulse, including the percussion wave (P), tidal wave (T), and diastolic wave (D). Additionally, attaching the LMSS to the left carotid artery, which is another common pulse detection site, we observed that the peak resistance signal was eight times that of the radial artery (Fig. 6c), with a smoother signal curve and a consistent pulsation period compared to the radial artery. The amplified carotid pulse signal (Fig. 6d) clearly showed the characteristic peaks of the arterial pulse. Therefore, the LMSS can be conveniently used on the neck and wrist to monitor pulse and heart rate, providing detailed clinical information. Placing the LMSS on the jaw enables the detection of mandibular movement (Fig. 6e, f). When repeatedly saying “Liquid Metal,” the sensor detected periodic multi-peak signals, distinguishing different syllables and pronunciations within a single cycle, demonstrating its potential applications in speech recognition and human-machine interaction.

Facial expressions play a crucial role in human emotional expression and communication, with different muscle movements resulting in various facial expressions. We attached LMSS to different areas of the face, including the corners of the eyes (Fig. 6g), the forehead (Fig. 6h), and the chin (Fig. 6i). Significant responses were observed for micro-expressions such as blinking, eyebrow raising, and smiling. Repeating these actions resulted in corresponding changes in the resistance signals. By detecting different facial muscle states with LMSS, it is possible to monitor human emotions and analyze psychological states.

Human movement is often achieved through the flexion and extension of various joints. The fingers are crucial for performing intricate tasks. To enhance wearing comfort, we fabricated a strain sensor for the index finger joint using AJP on a commonly used laboratory glove, enabling detection of finger bending (Fig. 6j). Additionally, the elbow and knee are frequently used joints in human movement. We attached LMSS to the elbow (Fig. 6k) and knee (Fig. 6l), where the $\Delta R/R_0$ increased during joint flexion and decreased during extension, demonstrating good repeatability, reliability, and reversibility. Furthermore, the LMSS exhibited distinct signal output patterns corresponding to different physical activities performed by the subject, such as when it was attached to the knee (Fig. 6m). The sensor's output signals could differentiate between jumping, stepping, walking, and running based on waveform, signal strength, and frequency. The use of LMSS for joint monitoring not only enables sensing of individual joint movements but also allows for the recognition and classification of different motion states. This technology has potential applications in activity monitoring and physical training.

Discussion

In summary, we have explored the printing of high-precision LM patterns using AJP with a minimum width of 12 μm . By adjusting the concentrations of PVP and DEG, ink dispersion, viscosity, surface tension, and volatility were systematically optimized, resulting in an LMI formulation suitable for AJP. We summarized the key steps and critical factors in AJP ink development. Notably, within the atomizable viscosity range, higher viscosities significantly suppressed impact spreading, resulting in narrower printed lines. Moreover, using this strategy, we successfully formulated CNTs, graphene, Fe, and SiC inks and achieved splatter-free AJP printing. This work enriches the methods for patterning LM and expands the range of materials compatible with AJP, providing a simple yet highly precise fabrication approach contributing to the development of flexible electronics.

Combining the high-resolution and patterning flexibility of AJP with the fluidity of LM, we designed fine-structured patterns to fabricate LMSS with both ultra-low $\varepsilon_{\text{emin}}$ and ultra-wide $\varepsilon_{\text{emax}}$ on flexible substrates. Narrower lines improved sensitivity and lowered detection limits, while complex patterns enhanced both sensitivity and sensing range via stress concentration and dispersion. Specifically, composite pattern I-sinusoid LMSS achieved a $\varepsilon_{\text{emin}}$ of 0.1% (30 μm) and a $\varepsilon_{\text{emax}}$ of 660% (198 mm); the S wave LMSS reached 0.0033% (1 μm) and 230% (69 mm); and the 60 μm line LMSS showed 0.0067% (2 μm) and 360% (108 mm). The ultra-broad effective sensing range of the LMSS allows for detecting physiological signals, speech, facial expressions, and joint motions, demonstrating the potential of our AJP-based LM patterning strategy for wearable and interactive electronics.

Methods

Ink preparation

All chemicals were used as received without further purification.

LMI ink. In 10 mL of anhydrous ethanol (AR, J&K Scientific, China) containing 0, 50, 100, 150, 200, 250, or 300 mg of polyvinylpyrrolidone (PVP, Mw = 58,000, Macklin, China), 9 g of eutectic gallium-indium alloy (EGaIn, Changsha Kunyong, China) was added. The composite solution was subjected to tip sonication (XO-3000W, Nanjing Xianou, China) at 500 W and 20 kHz for 30, 60, 90, and 120 min to obtain different LMI. During sonication, the sample temperature was maintained at -20°C using a cold-water bath. Subsequently, diethylene glycol (DEG, AR, J&K Scientific, China) at varying concentrations was added to the LMI to prepare printing inks with DEG concentrations of 0%, 5%, 10% and 15% v/v.

Other nanomaterial-based inks. CNTs or graphene inks were prepared by dispersing 50 mg of multi-walled CNTs (outer diameter: 30–80 nm, length: 0.5–2 μm , reagent grade, J&K Scientific, China) or graphene (XF002-1, XFNANO, China) into 10 mL of anhydrous ethanol containing 150 mg of PVP. The mixture was sonicated for 30 min using an ultrasonic cleaning bath, followed by the addition of 10% v/v diethylene glycol to obtain the final ink formulations. Similarly, 1 g of carbonyl iron powder ($<1.5\ \mu\text{m}$, Jiangsu Tianyi, China) or nano-sized SiC (40 nm, Macklin, China) particles was dispersed into 10 mL of deionized water containing 150 mg of PVP, sonicated for 30 min, and then mixed with 10% v/v diethylene glycol to yield the Fe ink and SiC ink, respectively.

Micro-deposition process

The AJP system was custom-built by our research group. The prepared LMI is atomized using a microporous ultrasonic atomization device, with nitrogen serving as both the inert sheath gas and atomization gas. A 150 μm nozzle and a working distance of 1 mm were employed.

LMI printing experiments. The carrier gas flow rate was set to 15 sccm, while the sheath gas flow rates were varied (20, 40, 60, 80, and 100 sccm), with a printing speed of 3 mm/s and a printing stage temperature of 90°C . Microscope slides were used as substrates.

Conductivity testing. A $2 \times 6\ \text{mm}$ rectangular pattern was printed twice onto a microscope slide at a carrier gas flow rate of 15 sccm, a sheath gas flow rate of 60 sccm, a printing speed of 3 mm/s, and a stage temperature of 90°C . After printing, the sample was dried on a heating plate at 100°C for 1 h. To activate the conductivity of the printed LM pattern, the sample, covered with polyethylene film, was repeatedly rolled with an iron rod.

Sensor performance and human motion sensing. A 30 mm straight line pattern was printed 9 times on 3M tape (VHB 4910A, 3M, USA) adhesive tape under the same conditions (15 sccm carrier gas flow rate,

60 sccm sheath gas flow rate, 3 mm/s printing speed, and 90°C stage temperature). The activated LM pattern was then encapsulated with 3M adhesive tape.

Morphological and electrical characterization

Material characterization. A scanning electron microscope (Gemini-SEM 300, ZEISS) and an optical microscope (VHX-S650E, KEYENCE) were used for morphological characterization. Line width measurements were based on the results obtained from a 3D optical profilometer and white light interferometer (Nexview NX2, Zygo). Rheological testing was conducted using a rotational rheometer (MCR302, Anton Paar). A video contact angle tester (OCA-25302, Dataphysics) was employed for surface tension and contact angle measurements. The stability of the ink was assessed using a UV-Vis spectrophotometer (UV-6100A, Shanghai Yuanxi), while the aerodynamic particle size of the aerosol was measured using an aerodynamic particle sizer (TSI 3321, TSI).

Electrical characterization. A four-point digital probe tester (M3, Suzhou Jingge Electronics Co., Ltd.) was used to measure the conductivity of the activated LMI (detailed in Appendix Note 2). An electrochemical workstation (CHI660E, Shanghai Chenhua) and a digital source meter (B2912A, Keysight) were used to assess the electrical properties and sensing performance of the LM patterns. The motorized stage (GCD-203300M, Daheng Optics, China) enabled 10 μm –200 mm displacements, while the precision stage (FMS115Z-200, Feinixs, China) covered 1 μm –1 mm.

Wearable human motion detection experiments

All procedures involving the on-skin attachment of liquid metal strain sensors for verifying human motion detection followed ethical guidelines and were reviewed and approved by the Medical Ethics Committee of Tsinghua University, project (THU-01-2025-1002). A healthy male participant, aged 32 and also a co-author of this study, was recruited to evaluate the wearable performance of the developed sensors. The data were collected, processed, and used with the participant's consent. Sex and gender differences were not specifically considered, as the primary aim was to assess the sensor's signal response to human motion rather than potential influences of sex or gender. These experiments were conducted solely to evaluate the performance of the strain sensors in capturing strain signals induced by human motion. No identifiable personal data were collected, and the study posed no physical or psychological risk. Partial facial features (such as eyes and lips) are shown in the manuscript to illustrate sensor placement and functional testing, and publication of these images was approved by the participant through written informed consent.

Reporting summary

Further information on research design is available in the Nature Portfolio Reporting Summary linked to this article.

Data availability

All data supporting the findings of this study are available within the paper and its Supplementary Information files. Source data are provided with this paper. Source data are provided as a Source data file.

References

1. Liu, S. et al. Strategies for body-conformable electronics. *Matter* **5**, 1104–1136 (2022).
2. Yadav, A. et al. Wearable strain sensors: state-of-the-art and future applications. *Mater. Adv.* **4**, 1444–1459 (2023).
3. Yao, S. et al. Nanomaterial-enabled flexible and stretchable sensing systems: processing, integration, and applications. *Adv. Mater.* **32**, 201902343 (2019).

4. Wang, H. et al. Carbon-based flexible devices for comprehensive health monitoring. *Small Methods* **7**, 2201340 (2023).
5. Shi, L. et al. A review of flexible strain sensors for walking gait monitoring. *Sens. Actuators A Phys.* **377**, 115730 (2024).
6. Si, Y. et al. Flexible strain sensors for wearable hand gesture recognition: from devices to systems. *Adv. Intell. Syst.* **4**, 202100046 (2022).
7. Heng, W. et al. Flexible electronics and devices as human–machine interfaces for medical robotics. *Adv. Mater.* **34**, 202107902 (2022).
8. Bai, Y. et al. Response regulation for epidermal fabric strain sensors via mechanical strategy. *Adv. Funct. Mater.* **33**, 202214119 (2023).
9. Lin, Y. et al. Ultrasensitive and highly stretchable bilayer strain sensor based on bandage-assisted woven fabric with reduced graphene oxide and liquid metal. *Chem. Eng. J.* **487**, 150777 (2024).
10. Zhai, W. et al. Stretchable, sensitive strain sensors with a wide workable range and low detection limit for wearable electronic skins. *ACS Appl. Mater. Interfaces* **14**, 4562–4570 (2022).
11. Qu, X. et al. Crack-based core-sheath fiber strain sensors with an ultralow detection limit and an ultrawide working range. *ACS Appl. Mater. Interfaces* **14**, 29167–29175 (2022).
12. Chen, J. et al. Design of flexible strain sensor with both ultralow detection limit and wide sensing range via the multiple sensing mechanisms. *Compos. Sci. Technol.* **213**, 108932 (2021).
13. Liu, Z. et al. Thickness-gradient films for high gauge factor stretchable strain sensors. *Adv. Mater.* **27**, 6230–6237 (2015).
14. Ratnayake, D. et al. Optimizing the conductivity of a new nanoparticle silver ink for aerosol jet printing and demonstrating its use as a strain gauge. *IEEE J. Flex. Electron.* **2**, 248–255 (2023).
15. Tian, B. et al. All-printed, low-cost, tunable sensing range strain sensors based on Ag nanodendrite conductive inks for wearable electronics. *J. Mater. Chem. C7*, 809–818 (2019).
16. Herbert, R. et al. Printed, soft, nanostructured strain sensors for monitoring of structural health and human physiology. *ACS Appl. Mater. Interfaces* **12**, 25020–25030 (2020).
17. Ji, J. et al. High Sensitivity and a wide sensing range flexible strain sensor based on the V-groove/wrinkles hierarchical array. *ACS Appl. Mater. Interfaces* **14**, 24059–24066 (2022).
18. Liang, B. et al. Direct patterning of carbon nanotube via stamp contact printing process for stretchable and sensitive sensing devices. *Nanomicro Lett.* **11**, 92 (2019).
19. Zhang, H. et al. Anisotropic, wrinkled, and crack-bridging structure for ultrasensitive, highly selective multidirectional strain sensors. *Nanomicro Lett.* **13**, 122 (2021).
20. Yun, Y. J. et al. Highly elastic graphene-based electronics toward electronic skin. *Adv. Funct. Mater.* **27**, 1701513 (2017).
21. Chun, S. et al. All-graphene strain sensor on soft substrate. *Carbon* **116**, 753–759 (2017).
22. Saeidi-Javash, M. et al. All-printed MXene–graphene nanosheet-based bimodal sensors for simultaneous strain and temperature sensing. *ACS Appl. Electron. Mater.* **3**, 2341–2348 (2021).
23. Zhu, J. et al. Recent progress in multifunctional, reconfigurable, integrated liquid metal-based stretchable sensors and standalone systems. *Prog. Mater. Sci.* **142**, 101228 (2024).
24. Qin, J. et al. Emerging advances of liquid metal toward flexible sensors. *Adv. Mater. Technol.* **9**, 2300431 (2024).
25. Lu, G. et al. Room-temperature liquid metals for flexible electronic devices. *Small* **20**, 2304147 (2024).
26. Wu, D. et al. Fast and facile liquid metal printing via projection lithography for highly stretchable electronic circuits. *Adv. Mater.* **36**, 2307632 (2024).
27. Chin, R. M. et al. Surface-engineered liquid metal particles for printing stretchable conductive composites with enhanced stability under different strain rates. *Adv. Mater. Technol.* **9**, 2301324 (2023).
28. Wang, S. L. et al. Highly stretchable liquid-metal based strain sensor with high sensitivity for human activity monitoring. *Mater. Lett.* **308**, 131277 (2022).
29. Chen, J. et al. Superelastic, sensitive, and low hysteresis flexible strain sensor based on wave-patterned liquid metal for human activity monitoring. *ACS Appl. Mater. Interfaces* **12**, 22200–22211 (2020).
30. Luo, Y. et al. Flexible liquid metal-based microfluidic strain sensors with fractal-designed microchannels for monitoring human motion and physiological signals. *Biosens. Bioelectron.* **246**, 115905 (2024).
31. Wu, Y. et al. Liquid metal-based strain sensor with ultralow detection limit for human–machine interface applications. *Adv. Intell. Syst.* **3**, 2000235 (2021).
32. Zahri, N. N. A. H. et al. Wearable strain sensors: design shapes, fabrication, encapsulation and performance evaluation methods. *Sens. Diagn.* **3**, 1635–1650 (2024).
33. Fan, J. A. et al. Fractal design concepts for stretchable electronics. *Nat. Commun.* **5**, 3266 (2014).
34. Wang, B. et al. Liquid metal microscale deposition enabled high resolution and density epidermal microheater for localized ectopic expression in *Drosophila*. *Adv. Mater. Technol.* **7**, 2100903 (2021).
35. Guo, H. et al. Fabrication of a flexible strain sensor with high-aspect-ratio liquid-metal Galinstan. *Adv. Mater. Technol.* **8**, 2200749 (2023).
36. Hu, G. et al. Maskless fabrication of highly conductive and ultra-stretchable liquid metal features through selective laser activation. *ACS Appl. Mater. Interfaces* **15**, 28675–28683 (2023).
37. Zhang, S. et al. High-fidelity conformal printing of 3D liquid alloy circuits for soft electronics. *ACS Appl. Mater. Interfaces* **11**, 7148–7156 (2019).
38. Xu, J. et al. Printable and recyclable conductive ink based on a liquid metal with excellent surface wettability for flexible electronics. *ACS Appl. Mater. Interfaces* **13**, 7443–7452 (2021).
39. Ma, J. et al. Shaping a soft future: patterning liquid metals. *Adv. Mater.* **35**, 2205196 (2023).
40. Ma, B. et al. A Versatile Approach for Direct Patterning of Liquid Metal Using Magnetic Field. *Adv. Funct. Mat.* **29**, 1901370 (2019).
41. Veerapandian, S. et al. Hydrogen-doped viscoplastic liquid metal microparticles for stretchable printed metal lines. *Nat. Mater.* **20**, 533–540 (2021).
42. Zhang, M. et al. Versatile fabrication of liquid metal nano-ink based flexible electronic devices. *Appl. Mater. Today* **22**, 100903 (2021).
43. Wilkinson, N. J. et al. A review of aerosol jet printing—a non-traditional hybrid process for micro-manufacturing. *Int. J. Adv. Manuf. Technol.* **105**, 4599–4619 (2019).
44. Fisher, C. et al. Aerosol-jet printed sensors for environmental, safety, and health monitoring: a review. *Adv. Mater. Technol.* **8**, 2300030 (2023).
45. Gamba, L. et al. Systematic design of a graphene ink formulation for aerosol jet printing. *ACS Appl. Mater. Interfaces* **15**, 3325–3335 (2023).
46. Iervolino, F. et al. Aerosol jet printing of a benzocyclobutene-based ink as adhesive material for wafer bonding application. *Adv. Mater. Interfaces* **10**, 2202183 (2022).
47. Feng, J. Q. et al. A quantitative analysis of overspray in Aerosol Jet® printing. *Flex. Print. Electron.* **6**, 045006 (2021).
48. Secor, E. B. Principles of aerosol jet printing. *Flex. Print. Electron.* **3**, 035002 (2018).
49. Avvaru, B. et al. Ultrasonic atomization: effect of liquid phase properties. *Ultrasonics* **44**, 146–158 (2006).
50. Robinson, C. S. Some factors influencing sedimentation. *Ind. Eng. Chem.* **18**, 869–871 (1926).
51. Liu, Y. et al. Water-processable liquid metal nanoparticles by single-step polymer encapsulation. *Nanoscale* **12**, 13731–13741 (2020).

52. Liu, S. et al. Ultrasonic-enabled nondestructive and substrate-independent liquid metal ink sintering. *Adv. Sci.* **10**, 2301292 (2023).
53. Jo, Y. et al. Printable self-activated liquid metal stretchable conductors from polyvinylpyrrolidone-functionalized eutectic gallium indium composites. *ACS Appl. Mater. Interfaces* **14**, 10747–10757 (2022).
54. Secor, E. B. Guided ink and process design for aerosol jet printing based on annular drying effects. *Flex. Print. Electron.* **3**, 035007 (2018).
55. Taccola, S. et al. Micro-scale aerosol jet printing of superparamagnetic Fe₃O₄ nanoparticle patterns. *Sci. Rep.* **12**, 17931 (2022).
56. Jabari, E. et al. Micro-scale aerosol-jet printing of graphene interconnects. *Carbon* **91**, 321–329 (2015).
57. Lohse, D. Fundamental fluid dynamics challenges in inkjet printing. *Annu. Rev. Fluid Mech.* **54**, 349–382 (2022).
58. Josserand, C. et al. Drop impact on a solid surface. *Annu. Rev. Fluid Mech.* **48**, 365–391 (2016).
59. Laan, N. et al. Maximum diameter of impacting liquid droplets. *Phys. Rev. Appl.* **2**, 044018 (2014).
60. Chen, S. et al. Transparent and waterproof ionic liquid-based fibers for highly durable multifunctional sensors and strain-insensitive stretchable conductors. *ACS Appl. Mater. Interfaces* **10**, 4305–4314 (2018).
61. Liu, L. et al. A Review on knitted flexible strain sensors for human activity monitoring. *Adv. Mater. Technol.* **8**, 2300820 (2023).
62. Amjadi, M. et al. Stretchable, skin-mountable, and wearable strain sensors and their potential applications: a review. *Adv. Funct. Mater.* **26**, 1678–1698 (2016).
63. Mao, L. et al. Configurable direction sensitivity of skin-mounted microfluidic strain sensor with auxetic metamaterial. *Lab Chip* **22**, 1630–1639 (2022).
64. Choi, D. Y. et al. Highly stretchable, hysteresis-free ionic liquid-based strain sensor for precise human motion monitoring. *ACS Appl. Mater. Interfaces* **9**, 1770–1780 (2017).

Acknowledgements

This work is supported by the National Natural Science Foundation of China (Grant No. 51961145303, M.Z.) and the Beijing Discipline Joint Construction Fund, Department of Mechanical Engineering, Tsinghua University (M.Y.).

Author contributions

M.Z. and B.X. conceived the research. B.X. designed and performed the experiments, collected and analyzed the data, and wrote the

manuscript. M.Z. and M.Y. supervised the research. W.C. contributed to the sensor application experiments and assisted with figure design. X.L., X.X., and W.L. assisted with data analysis. H.Z. helped design experiments and revised the manuscript. All authors reviewed and commented on the manuscript.

Competing interests

The authors declare no competing interests.

Additional information

Supplementary information The online version contains supplementary material available at <https://doi.org/10.1038/s41467-025-63023-y>.

Correspondence and requests for materials should be addressed to Ming Zhou.

Peer review information *Nature Communications* thanks the anonymous reviewers for their contribution to the peer review of this work. A peer review file is available.

Reprints and permissions information is available at <http://www.nature.com/reprints>

Publisher's note Springer Nature remains neutral with regard to jurisdictional claims in published maps and institutional affiliations.

Open Access This article is licensed under a Creative Commons Attribution-NonCommercial-NoDerivatives 4.0 International License, which permits any non-commercial use, sharing, distribution and reproduction in any medium or format, as long as you give appropriate credit to the original author(s) and the source, provide a link to the Creative Commons licence, and indicate if you modified the licensed material. You do not have permission under this licence to share adapted material derived from this article or parts of it. The images or other third party material in this article are included in the article's Creative Commons licence, unless indicated otherwise in a credit line to the material. If material is not included in the article's Creative Commons licence and your intended use is not permitted by statutory regulation or exceeds the permitted use, you will need to obtain permission directly from the copyright holder. To view a copy of this licence, visit <http://creativecommons.org/licenses/by-nc-nd/4.0/>.

© The Author(s) 2025